Research Square

Preprints are preliminary reports that have not undergone peer review.
They should not be considered conclusive, used to inform clinical practice,
or referenced by the media as validated information.

Influence of OPGW Structure on Ice-Melting Characteristics and Optical fiber Temperature under DC

Bo Zhou
State Grid Economic and Technological Research Institute Co., Ltd
Song Bao
China Energy Engineering Group Anhui Electric Power Design Institute Co., Ltd
Yunfei Shi
China Energy Engineering Group Anhui Electric Power Design Institute Co., Ltd
Chao Yang
China Energy Engineering Group Anhui Electric Power Design Institute Co., Ltd
Yue Zhu
zhuyue021231@hnu.edu.cn

Hunan University

Article

Keywords: Optical fiber composite overhead ground wire, ice melting, structural parameters, Joule heating, optical fiber temperature

Posted Date: November 23rd, 2026

DOI: https://doi.org/10.21203/rs.3.rs-11605436/v1

License: This work is licensed under a Creative Commons Attribution 4.0 International License.
Read Full License

Additional Declarations: No competing interests reported.

Article

Influence of OPGW Structure on Ice-Melting Characteristics and Optical fiber Temperature under DC

Bo Zhou[a], Song Bao[b], Yunfei Shi[b], Chao Yang[b], Yue Zhu[c]

[a] State Grid Economic and Technological Research Institute Co., Ltd., Beijing 102200, China
[b] China Energy Engineering Group Anhui Electric Power Design Institute Co., Ltd., Hefei 230601, China
[c] College of Electrical and Information Engineering, Hunan University, Changsha 410082, China

Corresponding author: Yue Zhu
Email: zhuyue021231@hnu.edu.cn
College of Electrical and Information Engineering, Hunan University, Changsha 410082, China

Abstract: Considering Joule heating, convective and radiative heat losses, ice-water phase change and dynamic evolution of air gap, a finite-element model is developed in this paper. The characteristics of electrical heat input, heat-transfer pathways, and fiber thermal response for OPGWs are analyzed. The effects of cable outer diameter, aluminum area fraction, and optical-unit location on ice-melting characteristics are investigated. It indicates that the air gap gradually expands during ice melting after applying a direct current (DC). Its thermal resistance would produce a nonlinear optical fiber temperature response, with a rapid initial increase followed by a slower rise. As the cable outer diameter increases from 13.6 to 16.8 mm, the ice-melting time increases from 3298.4 s to 4828.2 s whereas the optical fiber temperature decreases from 83.83 to 52.08 ℃. Increasing the aluminum area fraction from 0.30 to 0.52 increases the ice-melting time by 21.2% but decreases the optical fiber temperature by 23.90℃. The effect of outer diameter is governed jointly by electrical heat input and thermal and structural factors, whereas aluminum area fraction primarily affects ice melting by changing the equivalent resistance. The difference in ice-melting time with different optical-unit configurations is less than 1%, and their optical fiber temperature differences arises mainly from local heat-transfer pathways and thermal resistance variations. This study provides references for making ice-melting strategy and optimizing the OPGW structure.

Keywords: Optical fiber composite overhead ground wire; ice melting; structura l parameters; Joule heating; optical fiber temperature

1 Introduction

An optical fiber composite overhead ground wire (OPGW) integrates the lightning protection function of overhead ground wires with optical fiber communication. Its reliable

operation is critical to the reliability of transmission lines and the continuity of power system communication services [1]. Under low-temperature rain and snow conditions, ice accretion on the OPGW surface increases the mechanical load of the line, resulting in aggravated sag and non-uniform ice shedding. Severe icing may cause strand breakage, fitting failure, or communication outages [2]-[3]. DC ice melting works by injecting direct current into the conductive components of OPGW to generate Joule heat for heating, melting and shedding the ice layer, which constitutes an important technical measure for mitigating icing on transmission lines [4]-[5].

Previous studies have explored ice accretion and heat transfer processes of OPGW. To characterize ice formation and evolution, ice-accretion models coupling droplet impingement and freezing have been established; the influences of wind speed, wind direction, and ice thermophysical properties on ice morphology have been analyzed [6]-[8]. Existing research on ice melting predominantly focuses on the critical ice-melting current, ice-melting duration, and conductor temperature rise. On the basis of heat balance analysis, numerical simulation and experimental validation, prior works have clarified how conductor resistance, ice thickness, ambient temperature and heat dissipation conditions affect ice-melting efficiency [9]-[11]. For OPGWs, Luo [12] further incorporated the thermal response of the optical unit and its safe temperature limits, and observed significant temperature gradients during Joule heat transfer among metal strands, the optical unit and the ice layer. Moreover, the generation and expansion of air gaps substantially alter heat transfer paths and thermal resistance distribution throughout the melting process. Ashfaq [13] adopted coupled electromagnetic–thermal finite-element modelling to investigate the temperature distribution and optical-fiber thermal response of OPGWs with different steel-aluminum configurations under short-circuit conditions. Furthermore, Zhu [14] conducted thermal-structural coupling analysis and demonstrated that ice melting depends not only on the total heat input but also on the conductor cross-sectional structure, material thermophysical properties and local heat dissipation conditions. Nevertheless, most existing studies treat OPGW as a lumped integral model. In practice, OPGW designs differ considerably in outer diameter, metallic cross-sectional area, aluminum-to-steel ratio, number of stranding layers and optical-unit position. The separate contributions of these structural parameters to electric heat input and heat transfer pathways remain insufficiently understood.

In this paper, a transient heat transfer model of OPGW is established. The model incorporates Joule heating, ice-water phase change, air-gap evolution, as well as convective

and radiative heat losses from the outer ice surface. A three-layer parameterized OPGW structure is adopted to investigate the influences of cable outer diameter, aluminum area fraction, and optical-unit configuration. To separate the electrical heating effects induced by resistance variation from the heat transfer effects arising from geometric and material variations, two comparative working conditions are designed: constant identical current and identical heat input. Ice-melting duration, maximum optical fiber temperature, and cross-sectional temperature distribution are selected as evaluation indices. The mechanism by which the OPGW structure affects ice-melting duration and optical fiber temperature is elucidated.

2 Heat-Transfer mechanism for OPGW

2.1 OPGW Structure

OPGWs often comprise an optical unit and surrounding aluminum-clad steel (AS) strands. The stainless-steel tube protects the optical fibers whereas the AS strands provide electrical conduction, mechanical support and lightning protection. This study considers three-layer stainless-steel-tube OPGW structure with central or intermediate-layer optical units, as illustrated in Fig. 1.

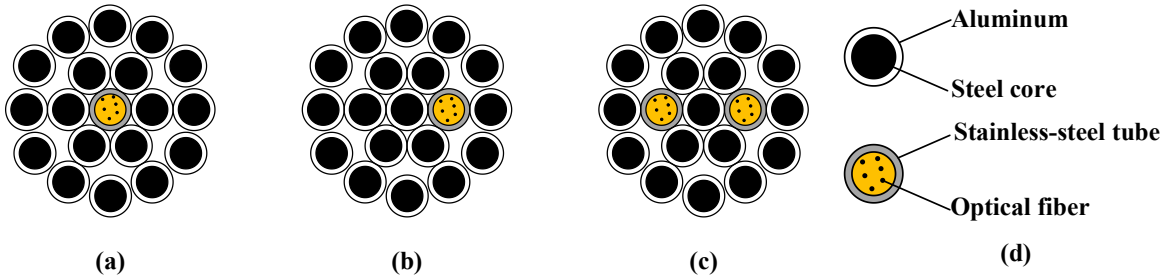

Figure 1. *Schematic of OPGW structure: (a) type a: one central optical unit; (b) type b: one intermediate-layer optical unit; (c) type c: two intermediate-layer optical units; (d) structural details of OPGW.*

The thermophysical and electrical properties adopted in the model are summarized in Table 1. The AS strands carry the ice-melting current, while the optical unit is assumed to be electrically non-conductive. Accordingly, the electrical conductivities of the stainless-steel tube and optical-fiber core are not considered.

Table 1. Material property for OPGW

Material	Specific heat capacity (J/(kg·K))	Thermal conductivity (W/(m·K))	Electrical conductivity (S/m)
Steel	475	58	4.032×10^{6}
Aluminum	900	201	3.030×10^{7}
Stainless-steel tube for optical fiber	475	17.5	——
Optical-fiber	703	1.38	——

The aluminum area fractions are selected according to the representative aluminum-clad steel wire grades. The aluminum and steel area fractions are listed in Table 2 [15].

Table 2. Fractions for aluminum and steel area

Grade	Aluminum area fraction (%)	Steel area fraction（%)	Electrical conductivity(%IACS)
LB23	30	70	23
LB25	34	66	25
LB27	37	63	27
LB30	43	57	30
LB35	52	48	35

2.2 Heat-Transfer Mechanism

DC ice melting relies on Joule heat generated within the conductive strands of OPGW to heat and melt the surrounding ice from the inside out. Heat propagates toward the optical unit and outward through the cable structure and air gaps to the ice layer and ambient air [16]. Figure 2 shows the temperature distribution and heat transfer domain.

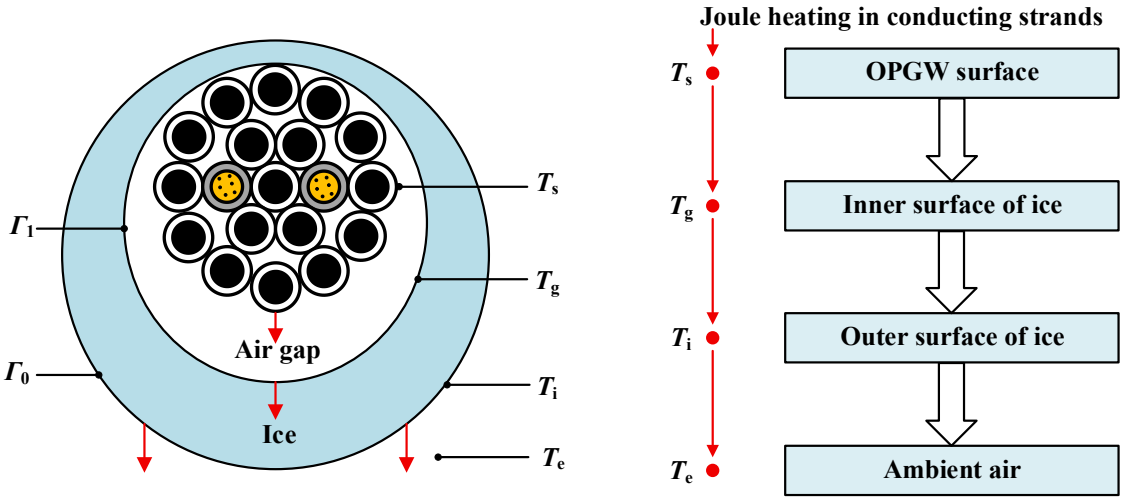

Figure 2. *Schematic of OPGW structure and heat transfer. (a) Structure of OPGW and thermal domain; (b) Heat-transfer pathway. T_s is the OPGW surface temperature, T_e is the ambient temperature, T_i and T_g are the temperatures at the outer ice boundary Γ_0 and inner ice boundary Γ_1, respectively. Θ denotes the computational cross-sectional domain comprising the OPGW, air gap, and ice layer.*

According to the heat-balance equation, the energy conservation equation during ice melting is [17-18]:

$$I^2 R_{eq}(t) = Q_{ext}(t) + \frac{d}{dt}\int_{\Theta} \rho Cp(T - T_e)dA + \rho_i L_f \frac{dA_m}{dt} \tag{1}$$

where I is the ice-melting current, R_{eq} is the resistance of the conductive components of the OPGW, Q_{ext} is the heat loss from the ice layer to the ambieknt environment, ρ and Cp are the material density and specific heat capacity, respectively. ρ_{i} is the ice-layer density, L_{f} is the latent heat of the ice-water phase change and A_{m} is the cumulative melted area of the ice-layer cross-section.

The terms Q_{ext} in Eq. (1) are expressed as follows:

$$Q_{ext}(t) = \int_{\Gamma_0} h_t (T_i - T_e)dl \tag{2}$$

where h_{t} is the heat-transfer coefficient between the outer ice surface and the ambient environment at time t.

To accurately describe the temperature-field distribution during ice melting and enable its quantitative solution and numerical simulation, governing equations for the dominant heat-transfer mechanisms are required. Since the air gap is small and fluid-flow effects within it are relatively weak, heat transfer in the computational domain Θ is approximated as conduction-dominated. The temperature field satisfies the heat-conduction equation:

$$\rho_k Cp_k \frac{\partial T_k}{\partial t} = \nabla_\perp \cdot (\lambda_k \nabla_\perp T_k) + q_k \tag{3}$$

where ρ_k is the density of each material, Cp_k is the specific heat capacity of each material, T_k is the temperature distribution function; λ_k is the thermal conductivity of each material, and q_k is the volumetric heat-source intensity within the computational domain Θ.

In the conductor layers, Joule heat is applied to the conductor regions as a volumetric heat source, with its intensity expressed as:

$$q_k = \frac{|J_k|^2}{\sigma_k} \tag{4}$$

where J_k is the current density, σ_k is the electrical conductivity. Given the current, the volumetric heat-source intensity depends on both cross-sectional area and electrical conductivity of conductor. The heat of OPGWs is not determined only by the total current.

The air gap is a key factor affecting temperature rise of optical fiber and ice-melting rate. As the inner ice surface melts, an asymmetric air gap gradually forms between OPGW and ice layer. To represent the evolving geometry while maintaining the stability of the moving-mesh solution, the evolution of melting interface is approximated using an eccentric circular air gap. For a small air gap, internal natural convection is weak, and the heat transfer inside the gap is dominated by heat conduction. The tendency for natural convection can be assessed using the Grashof number [19]:

$$Gr_\delta = \frac{2g(T_s - T_g)\delta^3}{v^2(T_s + T_g)} \tag{5}$$

where Gr_δ is the Grashof number of air-gap region; g is gravitational acceleration. T_s and T_g are the temperatures of outer surface and inner ice surface, respectively. v is the kinematic viscosity of air, and δ is the thickness of air gap between ice layer and OPGW.

Since the thermal conductivity of air is around 0.026 W/(m·K), which is much lower than that of ice, 2.31 W/(m·K), the formation of air gap substantially increases the equivalent thermal resistance between OPGW and inner ice surface. As the air gap expands, more heat would accumulate within the OPGW, while the effective heat flux transferred to the ice layer changes. It causes the nonlinear characteristics of optical fiber temperature as well as the interface propagation speed during ice melting [20].

3 Simulation study for Ice Melting of OPGW

3.1 Simulation model

The geometry of ice-covered OPGW is illustrated in Fig. 3. The computational domain comprises an optical unit consisting of stainless-steel tube and optical fiber, an aluminum-clad steel core layer, and an external ice layer.

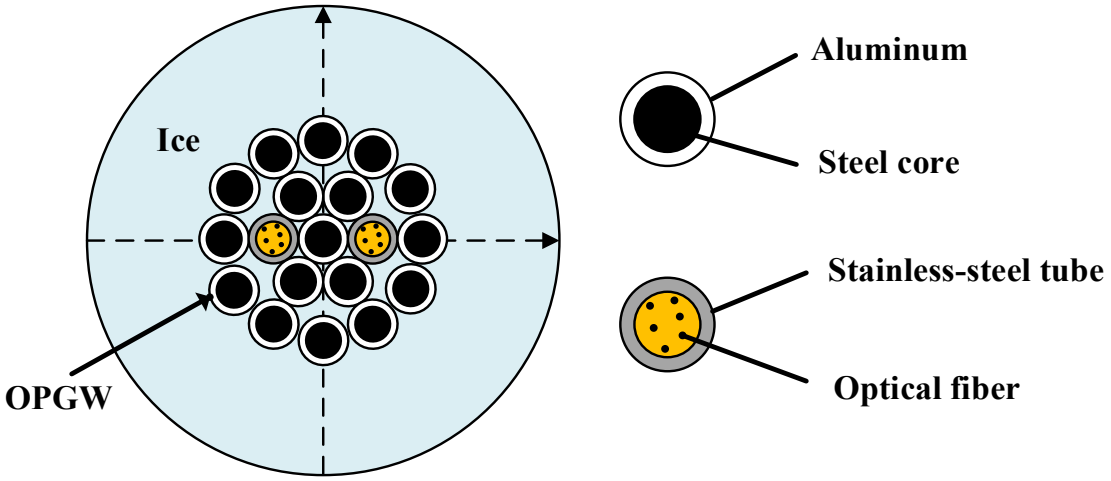

Figure 3. *Geometry of ice-covered OPGW. (a) Cross section of ice-covered OPGW; (b) Unit of OPGW.*

The convective and radiative heat exchange occur between the outer ice surface and the ambient environment. The boundary condition can be expressed as [21]:

$$-\lambda \frac{\partial T}{\partial n} = h_D(T_i - T_e) + \varepsilon \sigma_r (T_i^4 - T_e^4) \tag{6}$$

where ε is the emissivity of outer ice surface with 0.9, σ_r is the radiation constant, h_D is the convection heat-transfer coefficients. The convective heat-transfer coefficient includes the natural and forced convection heat-transfer coefficients and is expressed as:

$$\begin{cases} h_D = h_N + h_F \\ h_N = \dfrac{\lambda_{air} B (G_r P_r)^b}{D} \\ h_F = \dfrac{\lambda_{air} C (\mathrm{Re})^n (P_r)^{1/3}}{D} \end{cases} \tag{7}$$

where h_N, and h_F denote the natural convection and forced convection heat-transfer coefficients, respectively; λ_{air} is the thermal conductivity of air, D is the geometric diameter

after icing, B, b, C, and n are coefficients determined by Gr and Re ; Re, Gr, and Pr are the Reynolds, Grashof, and Prandtl numbers, respectively [22]-[23]. They are detailed as follows:

$$\begin{cases} Re = \dfrac{V_{\mathrm{a}} D \rho_{\mathrm{air}}}{\mu_{\mathrm{air}}} \\ Gr = \dfrac{2g(T - T_{\mathrm{e}})D^3}{\upsilon_{\mathrm{air}}^2 (T + T_{\mathrm{e}})} \\ Pr = \dfrac{\mu_{\mathrm{air}} C_{\mathrm{air}}}{\lambda_{\mathrm{air}}} \end{cases} \tag{8}$$

where g is gravitational acceleration, v_{air} is the kinematic viscosity of air, μ_{air} is the dynamic viscosity of air, C_{air} is the specific heat capacity of air, V_{a} is the wind speed, ρ_{air} is the density of air.

The current in OPGW is carried primarily by the aluminum-clad steel strands. To describe current sharing caused by the difference in electrical conductivity between the aluminum layer and steel core, these two regions in the entire OPGW are treated as axially parallel conducting paths. Let S_{m} denote the total effective metal cross-sectional area and f_{al} the aluminum area fraction. The effective cross-sectional areas of the aluminum layer and steel core are:

$$\begin{cases} S_{al} = f_{al} S_m \\ S_{fe} = (1 - f_{al}) S_m \end{cases} \tag{9}$$

The resistance is obtained from the electrical conductivities of the two materials, and the currents shared by the aluminum layer and steel core are determined from their parallel connection:

$$\begin{cases} r_{al} = 1/(\sigma_{al} S_{al}) \\ r_{fe} = 1/(\sigma_{fe} S_{fe}) \end{cases} \tag{10}$$

$$\begin{cases} I_{al} = r_{fe}/(r_{al} + r_{fe}) I_0 \\ I_{fe} = r_{al}/(r_{al} + r_{fe}) I_0 \end{cases} \tag{11}$$

The Joule heat is then applied separately to the aluminum-layer and steel-core regions as volumetric heat sources, with the heat-source intensities given by:

$$\begin{cases} q_{al} = I_{al}^2/(\sigma_{al} S_{al}^2) \\ q_{fe} = I_{fe}^2/(\sigma_{fe} S_{fe}^2) \end{cases} \tag{12}$$

where I_0 is the total current applied on OPGW. For a given current I_0, differences in equivalent resistance caused by structural changes are directly reflected in the total Joule heat input. Under the same heat-input-per-unit-length condition, the volumetric heat-source

intensities are adjusted to maintain a constant heating power, allowing the effects of structural dimensions, heat capacity, and heat-transfer paths on ice melting to be investigated.

To represent air-gap growth during ice melting, an initial air gap R_{g0} is introduced at the OPGW radius R_c, and the inner ice surface is represented by an eccentric circle. As the air-gap radius R_g increases, its center moves vertically, maintaining a small gap above OPGW while the lower gap continues to expand. The following geometric relations are used:

$$\begin{cases} R_{g0} = R_c \\ y_g = R_{g0} - R_g \\ s = 2(R_g - R_{g0}) \end{cases} \tag{13}$$

where s represents the equivalent downward displacement of ice layer from its initial position, and y_g is the coordinate of air-gap center relative to OPGW center. The propagation speed of melting interface is determined by the interfacial energy balance and can be expressed as a Stefan-type relation [24]-[25]:

$$2\pi \cdot R_g \cdot \rho_i L_f (\frac{dR_g}{dt}) = P_{melt} \tag{14}$$

where P_{melt} is the effective heat source during ice-water phase change. As the temperature field changes, P_{melt} and R_g are coupled, enabling a dynamically coupled solution of temperature field and phase change.

3.2 Mesh Analysis

A time-dependent solver is used for the computational model. The mesh in the solid OPGW domain remains fixed whereas the air-gap and ice-layer domains are allowed to deform freely. The inner surface of ice moves according to the eccentric-circle geometry specified in Eq. (13). To improve model convergence under large deformation, Winslow smoothing is applied to the freely deforming domains, and the mesh is locally refined at the initial air gap, melting interface, and regions near the OPGW. The maximum internal time-integration step is also limited to reduce the effect of interface displacement within a single step on the nonlinear iterations.

A free triangular mesh is used for the model. To verify the effect of mesh size on the computational results, four mesh schemes, i.e., normal, fine, finer, and extra fine, are compared. The fiber temperatures during ice melting are illustrated in Fig. 4. The optical fiber temperatures differ slightly. Since a finer mesh requires a longer computation time and

greater computational resources, the fine mesh scheme is selected for this model. The resulting mesh is shown in Fig. 5.

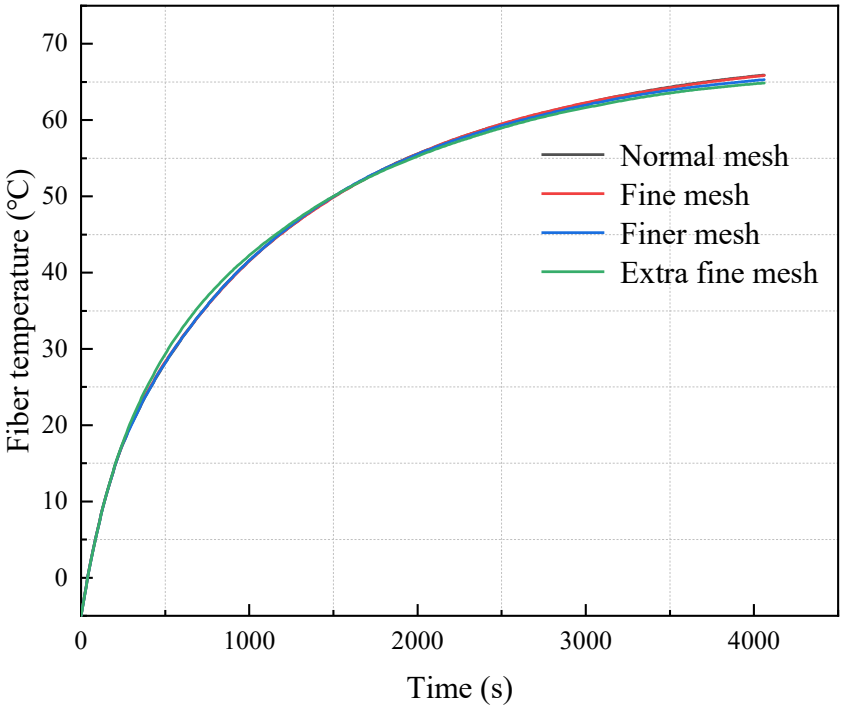

Figure 4. *Optical fiber temperature versus mesh size.*

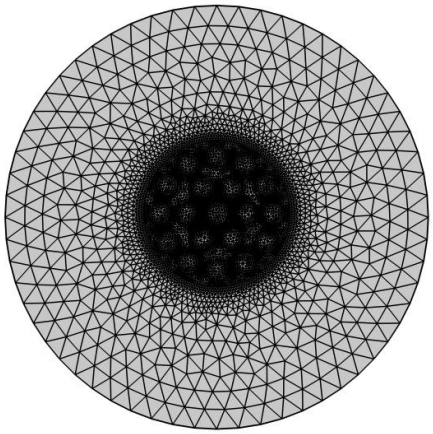

Figure 5. *Free triangular mesh used for OPGW.*

3.3 Results & Discussion

An OPGW-48B1-120 cable is selected in our study. The aluminum area fraction is 0.43. The operating conditions are set as follows: the wind speed V_a is 5 m/s, and the ambient temperature T_a is −5 ℃, the applied current I_0 is 300 A and the wire is covered by a uniform circular ice layer of 15 mm in thick. The computational results are illustrated in Fig. 6.

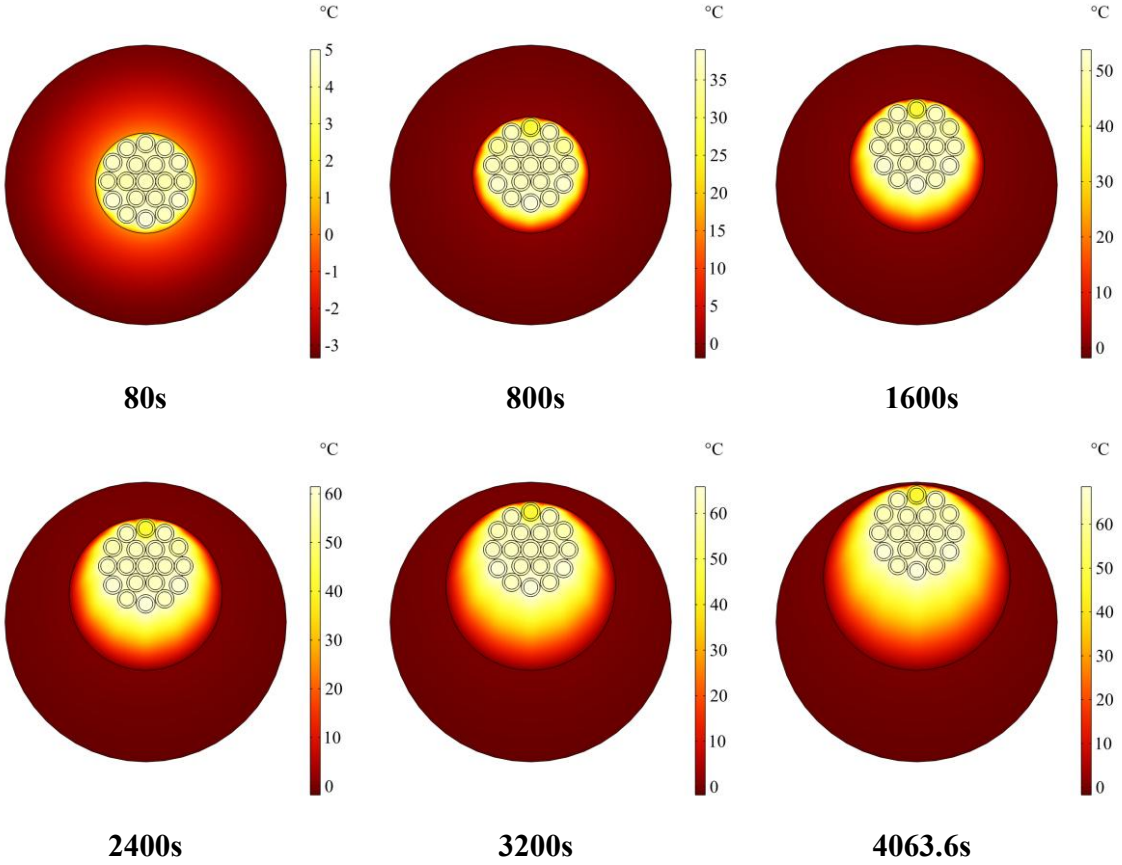

Figure 6. *Temperature field for OPGW during ice melting.*

Clearly, the high-temperature region and the position of melting interface change substantially as ice melts. As time goes, the air gap expands, and the eccentricity between OPGW and air gap also increases. The thermal resistance of air gap dominates the thermal resistance between the OPGW and its surroundings. Since the equivalent thermal resistance through the upper region is lower, the center of the high-temperature region shifts upward continuously. The upper region approaches the outer ice boundary, while a thicker low-temperature ice layer remains in the other directions, producing pronounced vertical asymmetry in ice melting.

Figure 7 shows the temperatures of outer ice surface and optical fiber. A large temperature difference persists between the two curves, indicating substantial thermal resistance to outward heat transfer from the OPGW interior. During the initial stage, the optical fiber temperature rises rapidly, primarily reflecting heat accumulation caused by the transfer of conductor Joule heat to the internal optical unit. As time goes, the difference between optical fiber and external ice layer temperature increases, and heat is gradually transferred to the ice layer and ambient environment. Meanwhile, the expansion of air gap weakens heat exchange between OPGW and ice layer, so more heat is transferred to the air

gap during the later stage. Consequently, the temperature of optical fiber exhibits a nonlinear response, which is rapid at initial stage but then slows down.

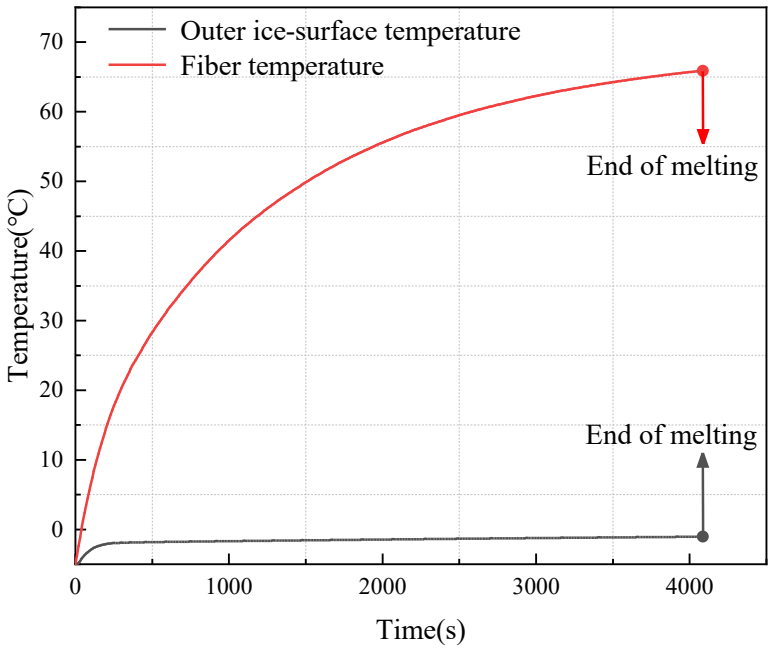

Figure 7. *Optical fiber temperature and outer ice-surface temperature.*

4 Sensitivity Analysis

The effects of cable outer diameter, aluminum area fraction, and optical-unit location are examined while ambient temperature, wind speed, ice thickness, and initial temperature are held constant. Two operating conditions are compared: the same ice-melting current and the same heat input. This comparison distinguishes effects associated with electrical heat input from those associated with thermal properties and heat-transfer pathways.

4.1 Effect of Outer Diameter of OPGW

Varying the outer diameter changes the conductive metal cross-sectional area, resistance, cable heat capacity, ice volume, and heat-transfer distance. The variation of optical fiber temperature versus outer diameters of OPGW is illustrated in Fig. 8. Given the same-current condition, smaller-diameter OPGWs exhibit faster increases in optical fiber temperature, shorter ice-melting times, and higher optical fiber temperatures at the end of ice melting. Increasing the outer diameter from 13.6 to 16.8 mm increases the ice-melting time from approximately 3298.4 to 4828.2 s and decreases the final optical fiber temperature from approximately 83.83 to 52.08 ℃. The ice-melting time increased monotonically across the diameter range.

In principle, the larger conductive cross-sectional area of a larger-diameter OPGW lowers its resistance and Joule heat generation. The greater ice quantity also increases the latent heat required for melting, while the longer heat-transfer pathway affects heat delivery to the ice layer. These effects contribute to the longer ice-melting time and lower optical fiber temperature of larger-diameter OPGWs. Smaller diameters therefore offer faster ice melting at the cost of higher optical fiber temperatures.

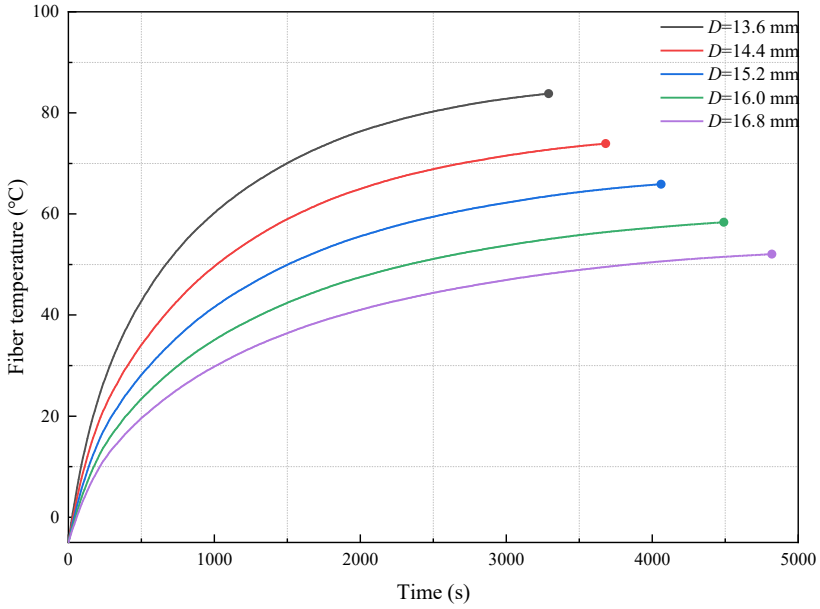

Figure 8. *Optical fiber temperature versus outer diameter of OPGW.*

The effect of outer diameter persists but is less pronounced, as shown in Fig. 9. As the outer diameter increases from 13.6 to 16.8 mm, the ice-melting time increases from approximately 3787.4 to 4374.8 s; the optical fiber temperature at completion decreases from approximately 68.45 to 62.66 ℃. The temperature curves are closer together than under the same-current condition. Maintaining the same heating power controls resistance-related differences in total heating power. The differences in ice-melting time and fiber temperature indicate that cable heat capacity, ice quantity, and heat-transfer distance also contribute to the diameter effect. Outer diameter therefore affects ice melting through both electrical heat input and the thermal response of the structure.

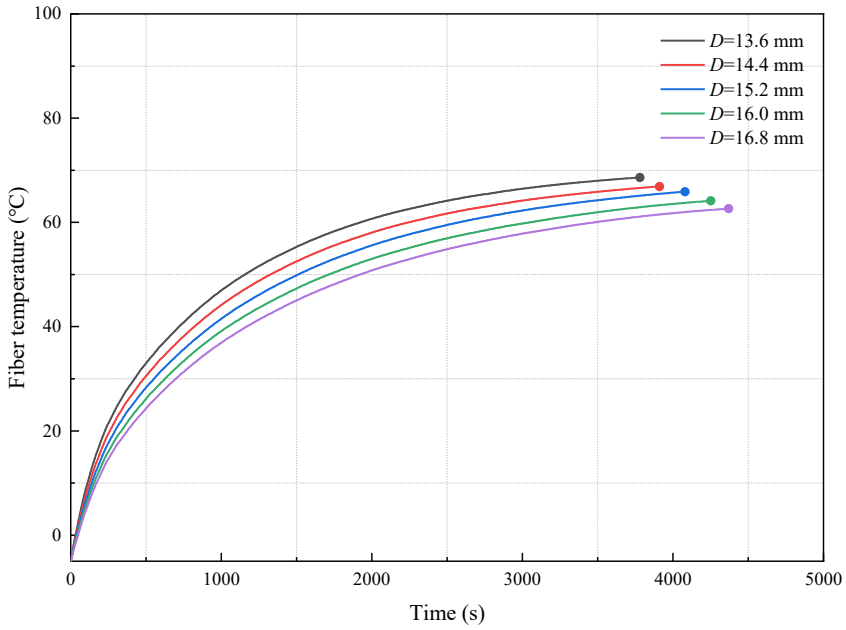

Figure 9. *Optical fiber temperature versus outer diameter of OPGW.*

4.2 Effect of Aluminum Area Fraction

Given the applied current, as illustrated in Figure 10, lower aluminum area fractions produce faster optical fiber temperature rises, shorter ice-melting times, and higher fiber temperatures at completion. Increasing the aluminum area fraction from 0.30 to 0.52 increases the ice-melting time from approximately 3567.6 to 4323.5 s, an increase of 21.2%, and decreases the optical fiber temperature from approximately 81.09 to 57.19 ℃, a decrease of 23.90 ℃. A lower aluminum area fraction corresponds to a larger steel-core fraction. Because steel is less electrically conductive than aluminum, this increases the equivalent resistance. At the same current, Joule heat generation therefore increases, raising the optical-unit temperature and increasing heat transfer to the ice layer. These results suggest that the effect of the aluminum-to-steel ratio on the equivalent electrical resistance is strongly nonlinear within a certain range.

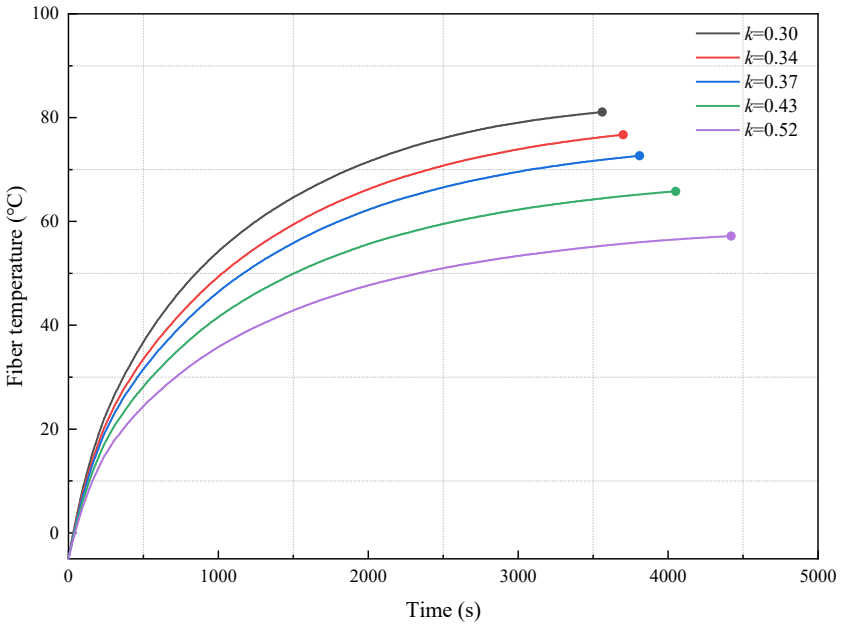

Figure 10. *Optical fiber temperature versus aluminum area fraction of OPGW.*

Figure 11 shows that the curves are close to each other. The ice-melting time ranges from 4056.7 to 4132.8 s, with a maximum deviation around 76.1 s. Optical fiber temperatures at completion differ by at most approximately 1.22 ℃ and are approximately 64.81 to 66.03 ℃. Given the heat input, resistance differences no longer directly change the total heat input. The remaining differences mainly reflect local heat-source distributions and material thermophysical properties. Their limited influence under unchanged cable dimensions and icing conditions indicates that aluminum area fraction affects ice melting primarily through its effect on equivalent resistance and, consequently, Joule heat generation under constant-current conditions.

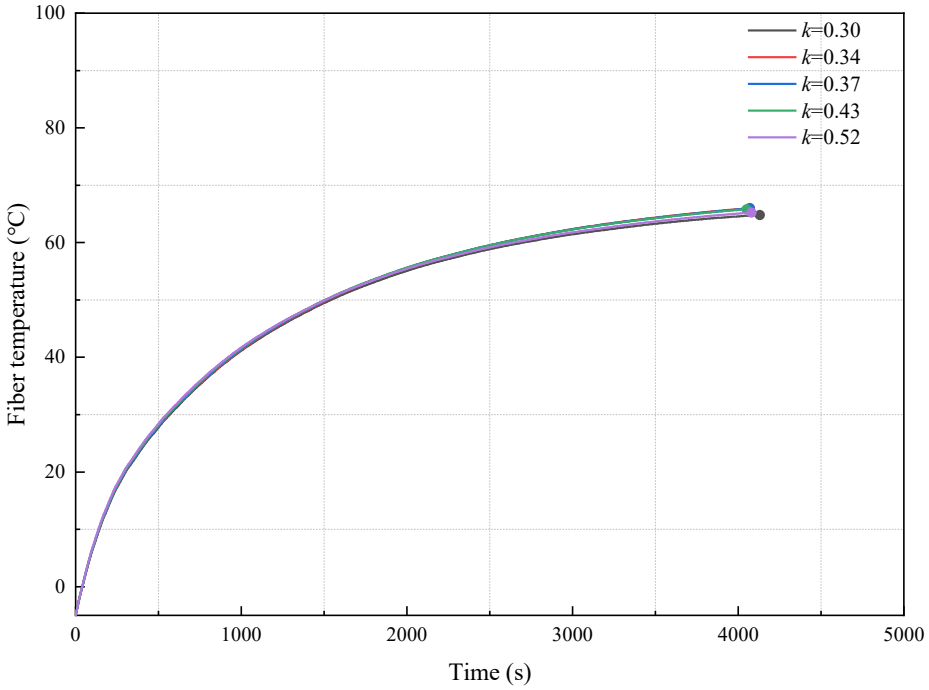

Figure 11. *Optical fiber temperature versus aluminum area fraction of OPGW.*

4.3 Effect of Optical-Unit Configuration

The configurations in Fig. 1 comprise one central optical unit (type a), one intermediate-layer optical unit (type b), and two intermediate-layer optical units (type c). Their outer diameter, environmental and icing conditions, and basic strand configuration are identical. Because an additional optical unit reduces the effective conductive metal area, these comparisons involve both optical-unit location and number, including their effects on resistance and local heat-transfer pathways.

Figure 12 shows that type c has the shortest ice-melting time, 4063.6 s, compared with 4216.3 s for type b and 4216.9 s for type a, a reduction of approximately 3.6%. Type c also has the highest optical fiber temperature at completion, 65.91 ℃, which is 4.24 and 2.13 ℃ higher than those of types b and a, respectively. The smaller conductive metal area of type c increases its equivalent resistance and Joule heating power, contributing to its shorter ice-melting time and higher final optical fiber temperature. Types a and b have nearly identical ice-melting times, but the final fiber temperature of type a is approximately 2.11 ℃ higher than that of type b. This comparison indicates that optical-unit location affects the fiber thermal response. The higher temperature of the central optical unit is consistent with greater local resistance to heat dissipation.

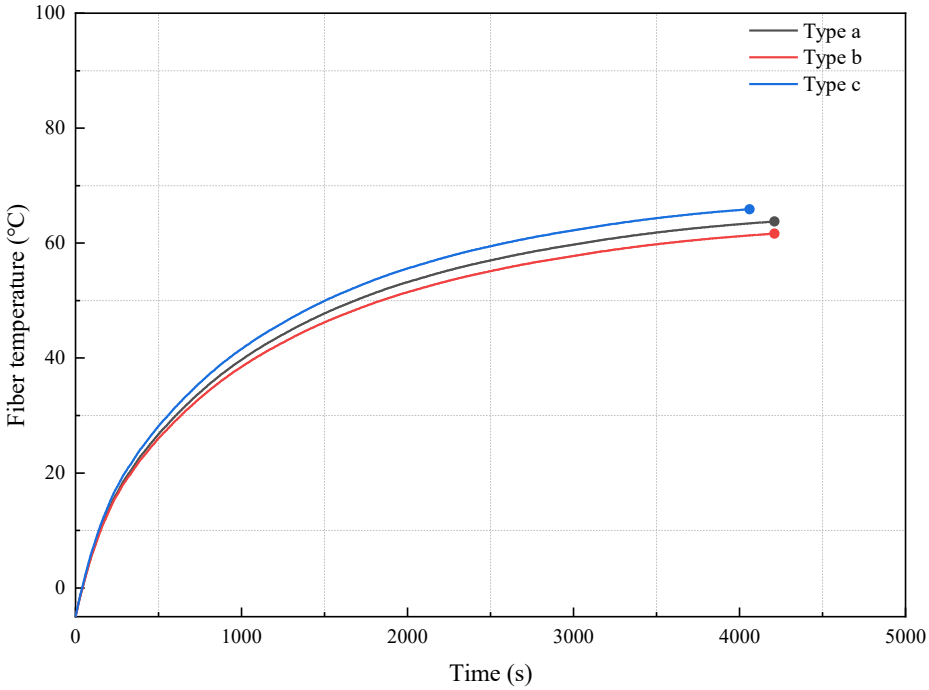

Figure 12. *Optical fiber temperature versus optical-unit configuration.*

Given the heat source, as illustrated in Fig. 13, the maximum ice-melting time difference among the three configurations is 35.3 s, approximately 0.9% of the total ice-melting time. Thus, equalizing the total heating power substantially reduces the differences in overall ice-melting performance associated with the conductive area. The final optical fiber temperature is the highest in type a, at 67.25 ℃, followed by type c at 65.91 ℃ and type b at 65.46 ℃. Type a is approximately 1.79 ℃ hotter than type b. With total heat input controlled, these temperature differences mainly reflect local heat-transfer pathways and thermal-resistance distributions. The higher temperature of the central optical unit suggests that its surrounding structure restricts outward heat transfer and favors local heat accumulation.

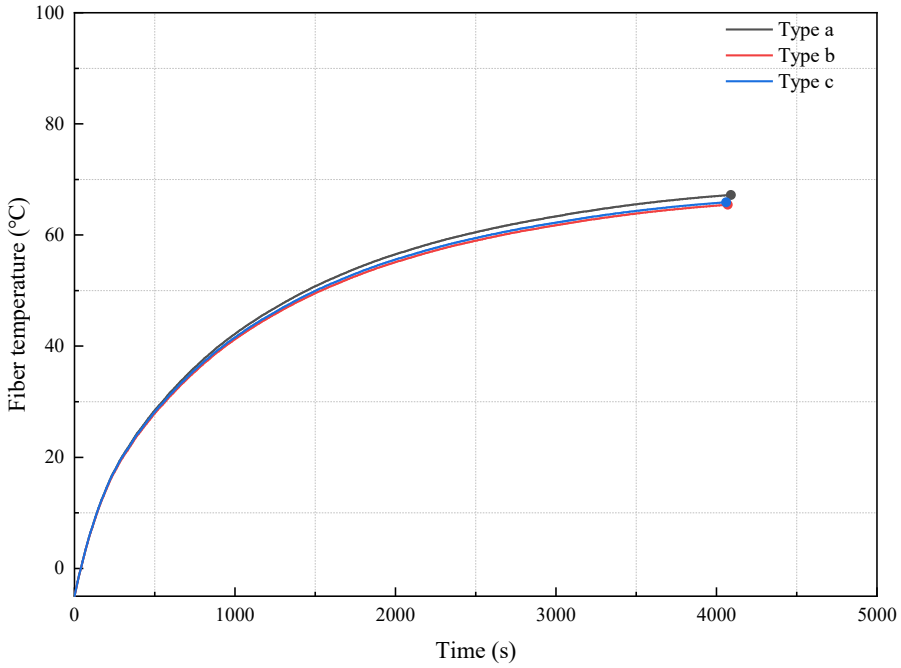

Figure 13. *Optical fiber temperature versus optical-unit configuration.*

In summary, OPGW structure affects ice melting through both electrical heat input and heat-transfer pathways. Maintaining the same heating power reduces the contribution of resistance-related heating differences and clarifies the remaining thermal effects.

5 Conclusion

(i) During the ice-melting process, as the inner surface of ice layer continuously melts, an asymmetric air gap forms and gradually expands between the OPGW and ice cover. The large thermal resistance of this air gap leads to gradual heat accumulation inside, resulting in a nonlinear variation of the optical fiber temperature: it rises rapidly in the early stage but slows down in the later stage. Meanwhile, the temperature field exhibits a pronounced vertically asymmetric distribution.

(ii) The influence of cable outer diameter on ice-melting characteristics involves both electrothermal input and thermal structural effects. At the same current, an increase in outer diameter reduces the resistance and Joule heat, while increasing the heat capacity, ice load and heat transfer distance. Consequently, the ice-melting duration is prolonged and the optical fiber temperature decreases. Under the same thermal power, this trend remains valid, yet the discrepancies among cables with different outer diameters are markedly reduced.

(iii) The aluminum area ratio affects the ice-melting process mainly by changing the equivalent resistance of OPGW. At the same current, reducing the aluminum area ratio increases Joule heat input and shortens the ice-melting time, but significantly elevates the

optical fiber temperature. When the thermal power is kept constant, the differences in ice-melting time and fiber temperature corresponding to different aluminum-to-steel ratios are substantially weakened, which indicates that its effect primarily originates from the variation in resistance.

(iv) The number and arrangement of optical units affect both the conductive area and local heat transfer paths. Under constant current, increasing the number of optical units raises the equivalent resistance and heat input due to the reduced conductive area, accelerating ice melting while increasing the fiber temperature. At the same thermal power, the ice-melting time of different structures is roughly comparable; nevertheless, the structure with a centrally located optical unit yields a relatively higher temperature. This demonstrates that local thermal resistance and heat transfer paths are critical determinants of the thermal response of optical fibers.

Data Availability

The datasets generated during and/or analysed during the current study are not publicly available due to confidentiality concerns but are available from the corresponding author on reasonable request.

Funding Statement

This work is financially supported by Science and Technology Foundation of State Grid Corporation of China (5500-202320188A-1-1-ZN).

Author Contributions

Bo Zhou: Supervision, Funding Acquisition. (equal). Song Bao: Conceptualization, Software, Writing – original draft. (equal). Yunfei Shi: Validation, Data curation. (equal). Chao Yang: Project Administration, Methodology. (equal). Yue Zhu: Formal Analysis, Writing – review & editing. (equal).

Competing Interests

The authors declare no competing interests.

References

[1] Iwata, M., Ohtaka, T., Goda, Y. et al. Melting and breaking characteristics of strands of high-strength and high-corrosion-resistant OPGW due to DC arc discharge simulating high-energy lightning strike. *Electrical Engineering in Japan* **214**, e23345 (2021).

[2] Zhang, Z., Zhang, H., Yue, S. et al. A review of icing and anti-icing technology for transmission lines. *Energies* **16**, 601 (2023).

[3] Rossi, A., Jubayer, C., Koss, H. et al. Combined effects of wind and atmospheric icing on overhead transmission lines. *Journal of Wind Engineering and Industrial Aerodynamics* **204**, 104271 (2020).

[4] Lei, M., Zhang, T., Li, Z. et al. Application status and development trends of DC ice-melting devices in China's power grid. *IET Smart Energy Systems* **2**(3), 171–180 (2026).

[5] Jiang, X., Meng, Z., Zhang, Z. et al. DC ice-melting and temperature variation of optical fibre for ice-covered overhead ground wire. *IET Generation, Transmission & Distribution* **10**, 352–358 (2016).

[6] Hou, H., Wang, Y., Bai, X. et al. Modelling icing growth on overhead transmission lines: Current advances and future directions. *Energy Conversion and Economics* **5**, 343–357 (2024).

[7] Fu, P., Farzaneh, M. & Bouchard, G. Two-dimensional modelling of the ice accretion process on transmission line wires and conductors. *Cold Regions Science and Technology* **46**, 132–146 (2006).

[8] Xu, F., Li, D., Gao, P. et al. Numerical simulation of two-dimensional transmission line icing and analysis of factors that influence icing. *Journal of Fluids and Structures* **118**, 103858 (2023).

[9] Fan, S., Jiang, X., Sun, C. et al. Temperature characteristic of DC ice-melting conductor. *Cold Regions Science and Technology* **65**, 29–38 (2011).

[10] Fan, S., Jiang, X., Shu, L. et al. DC ice-melting model for wet-growth icing conductor and its experimental investigation. *Science China Technological Sciences* **53**, 3248–3257 (2010).

[11] Zhu, Y., Huang, X., Zhao, L. et al. Thermodynamic model of critical ice-melting current on iced transmission lines. *Thermal Science* **23**, 3187–3198 (2019).

[12] Luo, T., Lin, S. & Sun, X. Dynamic thermal network model based temperature rise characteristics analysis for OPGW ice-melting process. *IEEE Transactions on Power Delivery* **41**, 1215–1228 (2026).

[13] Ashfaq, A., Khalique, U., Nadeem, A. & Rizvi, A. A. Comprehensive analysis of temperature distribution in OPGW cable considering ramifications of short circuit current. *Scientific Reports* **15**, 21949 (2025).

[14] Zhu, H., Han, Z., Xing, H. et al. DC ice-melting operation of the ground wire based on the characteristic investigation of the thermal structure coupling effect. *Electric Power Systems Research* **218**, 109181 (2023).

[15] State Administration for Market Regulation & Standardization Administration of China. Aluminium-clad steel wires for electrical purposes. GB/T 17937–2024 (2024).

[16] Hu, Q., Zhang, Y., Chen, X. et al. DC ice-melting temperature rise characteristics of OPGW and its influencing factors. *High Voltage Engineering* **51**, 2363–2373 (2025).

[17] Tan, L., Liu, Y., Yuan, Z. et al. Linear modeling analysis of the heat balance of the transmission line in high frequency critical ice melting state. *International Journal of Low-Carbon Technologies* **19**, 508–516 (2024).

[18] Wu, J., Wang, Q., Luo, D., Fang, J. & Sun, T. Feasibility exploration of nano-thermal rod applied to deicing of tunnel pavement in cold region. *Scientific Reports* **15**, 1528 (2025).

[19] Wang, S., Cheng, L., Tang, B. et al. Numerical analysis and experimental verification of optical fiber composite overhead ground wire (OPGW) direct current (DC) ice melting dynamic process considering gap convection heat transfer. *Energies* **18**, 2090 (2025).

[20] Jiang, X., Fan, S., Zhang, Z. et al. Simulation and experimental investigation of DC ice-melting process on an iced conductor. *IEEE Trans. Power Deliv*. **25**, 919–929 (2010).

[21] Jiang, X., Wang, Y., Shu, L. et al. Control scheme of the de-icing method by the transferred current of bundled conductors and its key parameters. *IET Generation, Transmission & Distribution* **9**(15), 2198–2205 (2015).

[22] Yang, G., Jiang, X., Liao, Y. et al. Research on load transfer melt-icing technology of transmission lines: Its critical melt-icing thickness and experimental validation. *Electric Power Systems Research* **221**, 109409 (2023).

[23] Huang, G., Wu, M., Liang, J. et al. Research on the DC Ice-Melting Model and Its Influencing Factors on the Overhead Contact Systems of an Electrification Railway. *Energies* **18**(5), 1028 (2025).

[24] Moench, S. & Dittrich, R. Influence of natural convection and volume change on numerical simulation of phase change materials for latent heat storage. *Energies* **15**, 2746 (2022).

[25] Tajik Jamalabad, M., Cortes, C., Pallarés, J. et al. Comparison of different numerical models for solidification of paraffin-based PCMs and evaluation of the effect of variable mushy zone constant. *Energies* **17**, 5982 (2024).